



ORIGINAL ARTICLE

Ni-Al layered double hydroxides electrodeposition from a chloride solution



Jun-jie Zhang^{a,b}, Ting-an Zhang^{a,b,*}, Sen Feng^a

^a School of Metallurgy, Northeastern University, Shenyang 110819, China

^b Key Laboratory of Ecological Metallurgy of Multi-metal Intergrown Ores of Ministry of Education, Northeastern University, Shenyang 110819, China

Received 1 April 2021; accepted 4 May 2021

Available online 11 May 2021

KEYWORDS

Ni-Al LDHs;
Electrodeposition;
NiCl₂-AlCl₃ solution;
Electrodeposition process

Abstract Ni-Al LDHs was electrodeposited from a NiCl₂-AlCl₃ solution. In order to analyze the electrodeposition process, electrolytes with initial Al content range of 0–20% were used. With increasing Al content in the sample, the preferred orientations of (0 0 3) and (0 0 6), increased crystallinity, and decreased interlayer spacing were observed from the XRD results. A dissolution–re crystallization of (0 0 3) plane was detected among the Ni-Al LDHs from the strongly alkaline solution soaking results, which was found to be conducted easily in high Al-containing samples. The pH of the Al-containing electrolyte was much lower than that of pure NiCl₂ solution because lower pH was needed to start a precipitation reaction in the AlCl₃-NiCl₂ solution. The electrodeposition yield and current efficiency were found to decrease obviously in the electrolytes with initial Al content higher than 10%, which was attributed to the increasing Al content in the sample and diffusion of the complex ions. The electrodeposition pattern was in-situ in the electrolyte initially containing 10% Al, then, it developed toward and off in-situ in electrolytes initially containing 0–10% and 10–20% Al.

© 2021 The Authors. Published by Elsevier B.V. on behalf of King Saud University. This is an open access article under the CC BY-NC-ND license (<http://creativecommons.org/licenses/by-nc-nd/4.0/>).

1. Introduction

Ni(OH)₂ is widely used as a catalyst for hydrogen evolution reaction, active material for Ni-based batteries, supercapacitors,

and precursor for the active material of lithium battery (Liu et al., 2019; Cheng et al., 2005; Wang et al., 2014; Xia et al., 2018). The increasing demand for the development of clean energy and energy storage devices for human beings has enhanced the application of Ni(OH)₂, although it has been studied for more than 100 years (Yuan et al., 2019; Hou et al., 2018; Pan et al., 2003; Peng et al., 2020).

Ni(OH)₂ has two crystalline forms, namely α-Ni(OH)₂ and β-Ni(OH)₂, which can be oxidized into γ-NiOOH and β-NiOOH by exchanging 1.67e and 1e per Ni atom (Yao et al., 2013; Jayashree and Vishnu, 2001; Li et al., 2018; Huang et al., 2018). Due to more electrons transferred in the oxidation/reduction process, a larger specific capacity can be

* Corresponding author at: School of Metallurgy, Northeastern University, Shenyang 110819, China.

E-mail address: zta2000@163.net (T.-a. Zhang).

Peer review under responsibility of King Saud University.



Production and hosting by Elsevier

expected for the α -Ni(OH)₂/ γ -NiOOH pair (Li et al., 2010; Vishnu Kamath et al., 1994). The α -Ni(OH)₂ form is, therefore, more attractive than β -Ni(OH)₂ (Jayashree and Vishnu, 1999; Miao et al., 2015). While, the easy conversion of α -Ni(OH)₂ to β -Ni(OH)₂ in a concentrated alkali solution not only restricts the widespread application of the former but also increases the difficulty of its preparation (Yao et al., 2013; Li et al., 2018; Jayashree and Kamath, 2011).

Several methods have been developed to prepare α -Ni(OH)₂ (Li et al., 2018; Vishnu Kamath et al., 1994; Subbaiah et al., 2002). Among them, electrodeposition is the most commonly used due to its advantages of cheapness, short processes, and good product performances (Subbaiah et al., 2002; Murthy et al., 1996; Ash et al., 2015). Ni(NO₃)₂ is an important raw material for α -Ni(OH)₂ electrodeposition and has been studied extensively over the past decades (Jayashree and Vishnu, 1999; Ash et al., 2015). However, the high OH⁻ and electron ratio (1.25:1) during the Ni(NO₃)₂ electrolysis contributes to a highly alkaline atmosphere around the cathode (Streinz et al., 1995; Zhang et al., 2021), which leads to the formation of β -Ni(OH)₂. Thus, Jayashree (Jayashree and Vishnu, 1999) demonstrated that a tough condition of high concentration and temperature (≥ 1 M and 60 °C) and low current density and pH (< 1.3 mA/cm² and ~ 1.7) was needed for the electrodeposition of α -Ni(OH)₂ from the system. Meanwhile, the formation of NH₃ by the cathodic reaction of Ni(NO₃)₂ electrolysis has a harmful effect on the electrolyte, which, in turn, affects the following reactions (Sasaki and Yamashita, 1998).

To enhance the stability of α -Ni(OH)₂ in concentrated alkali solution, the partial substitution of nickel ion in the α -Ni(OH)₂ lattice with other metal ions was performed (Li et al., 2012; Nethravathi et al., 2007; Demourgues Guerlou and Delmas, 1993; Demourgues Guerlou and Delmas, 1996; Chen et al., 2002). Among the used metal ions, Al is the most attractive due to its high stability in the trivalent state and low cost (Pan et al., 2003; Vishnu Kamath et al., 1994; Hu et al., 2011). The Al-substituted α -Ni(OH)₂ (Ni-Al LDHs) with the general formula of [Ni_{1-x}Al_x(OH)₂]_yA_m·mH₂O (A is an anion depending on the system used for preparation) is a type of α -Ni(OH)₂, in whose lattice partial Ni atoms are substituted by Al atoms (Li et al., 2016; Gualandi et al., 2015; Shangguan et al., 2015; Liu et al., 1999). The precipitation process of Ni-Al LDHs involves the precipitation of Ni²⁺ and Al³⁺ ions. The solubility product constant (K_{sp}) of Ni(OH)₂ (5.5×10^{-16}) is far different from that of Al(OH)₃ (1.3×10^{-33}), and the former has been reported to adhere to the electrode and the latter presents to be amphoteric (Subbaiah et al., 2002; Gualandi et al., 2015). Besides, the electrochemical processes are inherently complex. Thus, the chosen electrodeposition system, Ni²⁺-Al³⁺ concentrations in the system, etc., can affect the experimental results and lead to a failure in the preparation of the desired material, which limits the widespread use of electrodeposition in the formation of Ni-Al LDHs.

To resolve the existing problems in the electrodeposition of α -Ni(OH)₂ from Ni(NO₃)₂ solution, NiCl₂ was proposed as an alternative to Ni(NO₃)₂. Yao et al. proved the feasibility of α -Ni(OH)₂ electrodeposition from the pure water solution of NiCl₂ (Yao et al., 2019). Our previous work dealt with the formation of metal byproduct and β phase from a simple

membrane electrolysis system using ethanol–water mixture as the solvent (Zhang et al., 2021). It is necessary to thoroughly understand the electrodeposition process in order to remove its limitation in the preparation of Ni-Al LDHs. Analyzing the electrodeposition process can be helpful to understand the conditions required for the electrochemical reaction in order to establish the reasonable control needed to obtain the desired sample. However, few efforts were devoted to this aspect.

Considering the limitations of α -Ni(OH)₂ electrodeposition from Ni(NO₃)₂ solution and the synthesis of Ni-Al LDHs by electrodeposition, the electrodeposition of Ni-Al LDHs was proposed to occur from a NiCl₂-AlCl₃ solution in this study. An insight into the electrodeposition process of Ni-Al LDHs from chloride solution was also achieved in the present work.

2. Experimental

2.1. Preparation of the electrodeposition system and synthesis of the samples

NiCl₂·6H₂O (Analytical reagent, AR), AlCl₃·6H₂O (AR), and anhydrous ethanol (AR) were used as purchased from commercial sources. Pure water and water–ethanol mixture at a volume ratio of 1:1 separately served as the solvents for the anolyte and catholyte (Zhang et al., 2020). The corresponding solutes were identical in both cases. Electrodepositions were carried out in an electrolyte with a concentration of 0.2 M (x M NiCl₂ + (0.2-x) M AlCl₃) under a current value of 420 mA (15 mA/cm²). The value of x was adjusted to prepare the electrolytes with initial Al³⁺/(Al³⁺ + Ni²⁺) molar ratios of 0, 5, 10, 15 and 20%. Based on the Al content in the initial electrolyte, the resultant samples were labeled from α -Ni(OH)₂-0 to α -Ni(OH)₂-20, respectively.

The electrodeposition system was composed of a middle-set cathode chamber and two side-set anode chambers, as shown in Fig. 1. The chambers were separated using a cation-exchange membrane (CEM, HTECH-18231123, HUAMO TECH, China). The electrodes were fixed in the electrolytic cell to form a constant distance of 3 cm between the anode and cathode. The 304 stainless-steel cathode had a size of 35 × 90 × 1 mm (LHW) and the iridium & ruthenium coated titanium anode had a size of 17.5 × 90 × 1 mm (LHW) (Zhang et al., 2021; Zhang et al., 2020). The electrolytic cell and anode sheets were pretreated with anhydrous ethanol twice to remove organic residues, along with 5% hydrochloric acid once to remove metals and deionized water five times to remove ions. The fresh CEM was immersed in 0.2 M NiCl₂ solution for a whole night so that it swelled completely. The cathode was treated with 5000-mesh sandpaper to form a mirror-like face, which was further cleaned with deionized water five times to remove attachments after pretreatment in the same way with the anode. The synthesized precipitate both falling to the bottom of the cathodic chamber and adhering on the cathode surface were collected, washed with deionized water, filtered through a filter membrane with a bore diameter of 22 μ m, dried to a constant weight, weighted by an electronic balance (accuracy of 0.1 mg), and ground in a mortar (Zhang et al., 2021).

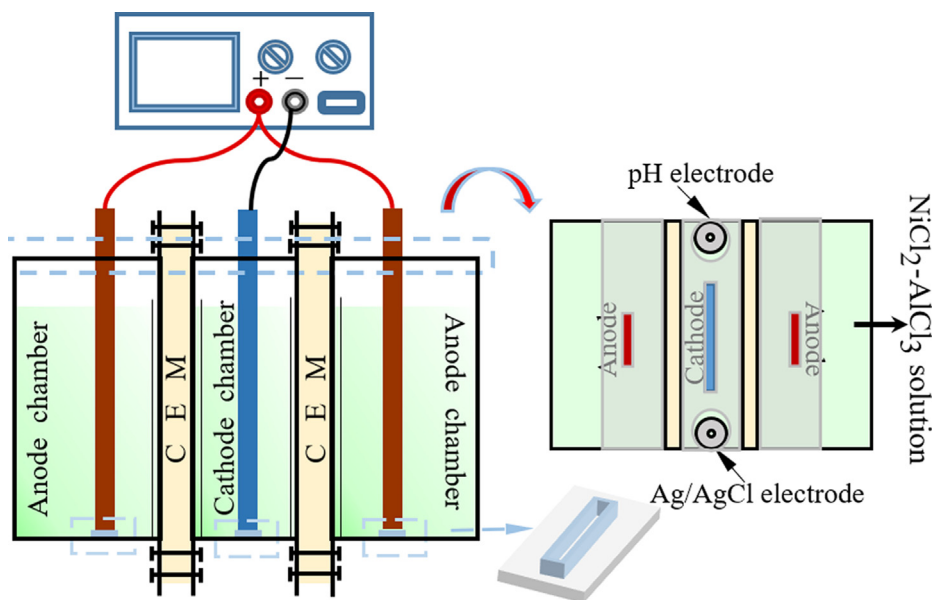


Fig. 1 Setup for the electrodeposition system.

2.2. Measurement of the electrodeposition system

The cathode potential vs. Ag/AgCl was recorded using the Agilent digital multimeter (Agilent, 34470A, USA) for every 0.5 s. The variations in the cell voltage were monitored by the DC power supply (eTM, L3055PL, China) for every 60 s. The pH of the catholyte was regulated by an acidimeter (LEICI, PHS-3E, China) for every 5 min. The pH electrode and Ag/AgCl electrode were on both sides of the cathode at a separation of 2.5 cm, as shown in Fig. 1.

The cyclic voltammetry (CV) measurement with respect to an Ag/AgCl electrode for the electrodeposition system was performed in a self-assembled three-electrode system using an electrochemical workstation (Zennium-pro, Zahner PP211, Germany). The working and counter electrodes were used as those mentioned in the literature (Zhang et al., 2021). The concentration of the electrolyte was 50 mM (y mM NiCl_2 + $(50-y)$ mM AlCl_3) and used the same solvent as that taken for the catholyte in the electrodeposition system. The cathodic sweep followed by the anodic sweep was performed at 30 mV/s.

2.3. Characterization of the samples

The Ni and Al contents in the samples were obtained by inductively-coupled plasma atomic emission spectroscopy (ICP, Leeman Prodigy XP, USA). The phase of the sample was determined by its X-ray diffraction patterns (XRD) observed using an X-ray diffractometer (Bruker D8, USA) at 40 kV and 40 mA ($\text{CuK}\alpha$ radiation, $\lambda = 1.54 \text{ \AA}$). To eliminate the influence of the sample mass on the XRD test, 100 mg of the powder sample was pressed to a disc with a diameter of 13 mm under 6 MPa. The Fourier-transform infrared spectroscopy (FT-IR) of the samples was performed using an infrared spectrometer (Nicolet iS50, USA). The particle size distribution measurement of the samples was performed using the Mastersizer 3000 Laser particle size analyzer made in the

UK. The stability of the sample was investigated by immersing 500 mg of each new sample in 6 M KOH (100 mL) at ambient temperature for several days.

3. Results and discussion

3.1. Physical and chemical characteristics of the samples

3.1.1. Phase features of the samples

Fig. 2a shows the Al content in the samples synthesized from the electrolyte initially containing 0–20% Al. A higher Al content was observed in the samples than those mentioned in the initial raw materials, which was different from that observed by chemical precipitation. By chemical precipitation, the samples shared a similar Ni/Al ratio as that in the raw materials (Miao et al., 2015; Shangguan et al., 2015; Shi et al., 2020).

The XRD patterns of the samples are shown in Fig. 2b. According to the standard card 00–038–0715, the phase characteristic similar to that of $\alpha\text{-Ni}(\text{OH})_2 \cdot 0.75\text{H}_2\text{O}$ was observed in the XRD patterns of all the samples, confirming the synthesis of $\alpha\text{-Ni}(\text{OH})_2$. In the five XRD patterns shown in Fig. 2b, no visible characteristic peaks related to $\text{Al}(\text{OH})_3$ were detected, indicating that the Al ion was successfully inserted into the lattice of $\alpha\text{-Ni}(\text{OH})_2$.

The (0 0 3) and (0 0 6) diffractions showed a decrease in broadening and an increase in intensity with the increasing Al content in the samples, as shown in Fig. 2b. This suggested that the Ni-Al LDHs preferred the (0 0 3) and (0 0 6) orientations. When the Al content in the sample ranged of 0–15%, the intensity of the diffraction peak was lower than that of the (0 0 6) plane. When the Al content in the sample increased to 20%, an opposite result was observed, which was thought to be related to the preparation method, the interlayer species and the Al content in the sample. Meanwhile, the diffraction peaks belonging to (0 0 3), (0 0 6), (1 0 1), and (1 1 0) planes moved toward the low 2θ direction, indicating a reduced crystal spacing in the direction perpendicular to these planes. In

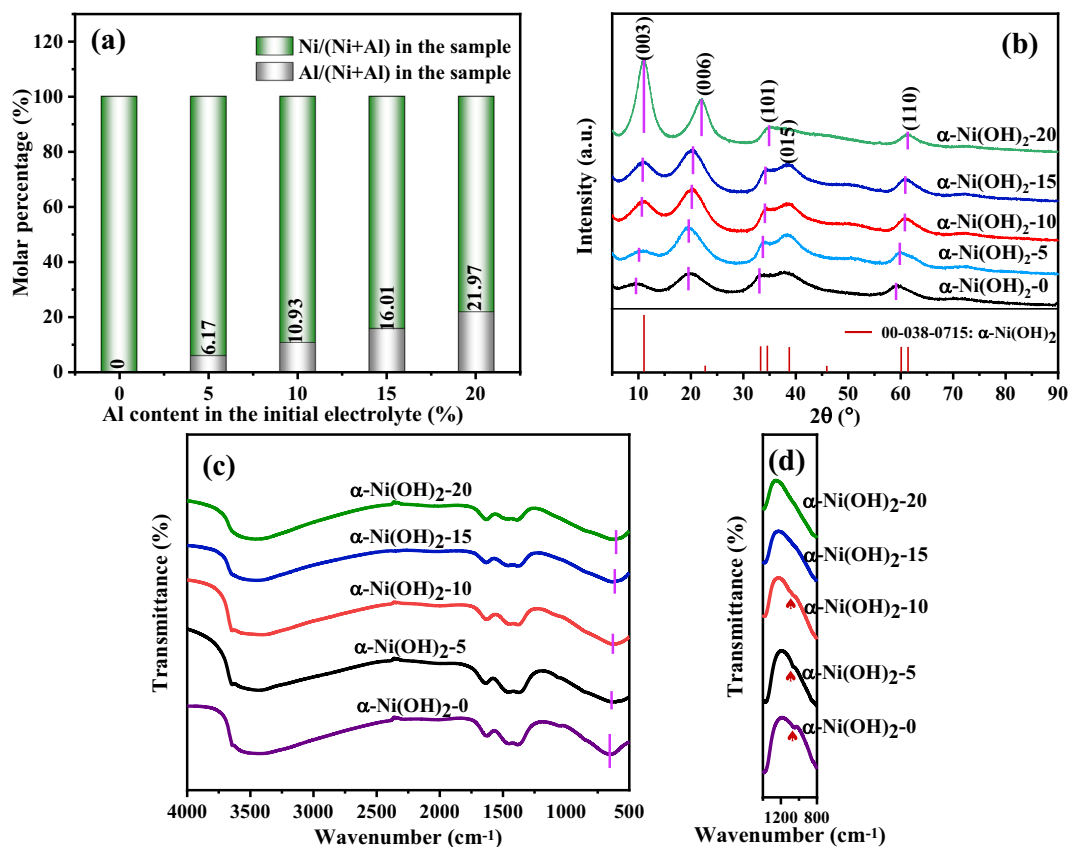


Fig. 2 (a) Al content, (b) XRD patterns, (c) FT-IR spectra of the samples and (d) the FT-IR spectra of the samples with the wavenumber between 1400 and 800 cm^{-1} .

particular, the distance between the (0 0 3) planes was commonly used to represent the interlayer spacing, which can be calculated on the basis of Bragg's equation (Shangguan et al., 2015). As tabulated in Table 1, $d_{(0\ 0\ 3)}$ was found to decrease from α -Ni(OH)₂₋₀ to α -Ni(OH)₂₋₂₀, indicating a decrease in the interlayer spacing with the increasing Al content in the samples as well as raw material solutions. It may be ascribed to the smaller radius of Al^{3+} ($r_s = 53.5$ pm) compared to Ni^{2+} ($r_s = 69$ pm). The full width at half maximum (FWHM) listed in Table 1 for the (0 0 3) planes was decreased from α -Ni(OH)₂₋₀ to α -Ni(OH)₂₋₂₀, indicating an increase in crystallinity with the Al content in the samples. The calculated grain size based on the (0 0 3) plane ($D_{(0\ 0\ 3)}$) (Shangguan et al., 2015) and mean particle size (D_{50}) listed in Table 1 were enhanced from samples α -Ni(OH)₂₋₀ to α -Ni(OH)₂₋₂₀, which was related to the increasing crystallinity of the samples.

To provide a supplement for phase determination by the XRD patterns of the samples, the FT-IR observations were performed. The recorded FT-IR spectra are presented in Fig. 2c. The broad band at approximately 3490 cm^{-1} is characteristic of the stretching vibration of the H-bonded OH⁻ groups, representing the intercalated H₂O molecules in the interlayer spacing (Pan et al., 2003; Huang et al., 2018; Jayashree and Kamath, 2011; Fang et al., 2019). The absorptions at about 1680 cm^{-1} and 1360 cm^{-1} are assigned to the bending vibration of the water molecule and vibration of the intercalated CO_3^{2-} (Li et al., 2010; Miao et al., 2015; Jayashree and Kamath, 2011). The vibration located at about 680 cm^{-1} is associated with the vibration of the in-plane Ni—O—H bond (Zhang et al., 2021; Shangguan et al., 2015; Zhang et al., 2020). The FT-IR analysis demonstrated that the samples exhibited a layered structure stacked by Ni(OH)₂

Table 1 Data summary of the samples from their XRD patterns and particle size analysis.

Samples	$2\theta/(0\ 0\ 3)$	$d_{(0\ 0\ 3)}/\text{nm}$	FWHM of (0 0 3)	$D_{(0\ 0\ 3)}/\text{nm}$	$D_{50}/\mu\text{m}$
α -Ni(OH) ₂₋₀	9.43	0.937	3.82	0.36	12.22
α -Ni(OH) ₂₋₅	10.02	0.882	3.56	0.39	17.47
α -Ni(OH) ₂₋₁₀	10.57	0.836	3.45	0.40	19.51
α -Ni(OH) ₂₋₁₅	10.80	0.818	3.17	0.43	24.80
α -Ni(OH) ₂₋₂₀	10.98	0.805	2.86	0.48	27.61

layers, with H₂O molecules and CO₃²⁻ in the interlayer spacing. These are termed as the α -Ni(OH)₂ form. In particular, a negative move was observed for the vibration of the in-plane Ni—O—H bond with increasing Al content in the sample, as seen from the vibration at about 680 cm⁻¹ for α -Ni(OH)₂₋₀ to α -Ni(OH)₂₋₂₀. In pure α -Ni(OH)₂, this vibrational signal was attributed entirely to the vibration of in-plane Ni—O—H. However, the vibrational signal at a similar location in Ni—Al LDHs may be ascribed to a combinative vibration of in-plane Ni—O—H at about 680 cm⁻¹ and Al—O—H at about 520 cm⁻¹ (Shi et al., 2020). The vibration component related to Al—O—H increased with the increasing Al content in the samples. Thus, the vibration at about 680 cm⁻¹ moved toward a low wavenumber with the increasing Al content in the sample. Notably, the anions in the raw materials were reported can be intercalated in the interlayer of α -Ni(OH)₂ (Li et al., 2010; Li et al., 2016; Gualandi et al., 2015). Therefore, Cl⁻ should be able to intercalated in the interlayer of Ni-Al LDHs synthesized in the present work. As seen from Table 2, there were Cl⁻ in the samples, and its content almost showed a decreasing trend from α -Ni(OH)₂₋₀ to α -Ni(OH)₂₋₂₀. To verify the intercalation of Cl⁻, the FT-IR spectrum of the samples between wavenumber 1400–800 cm⁻¹ was selected in Fig. 2d. A tiny vibration at approximately 1043 cm⁻¹ can be obviously observed from the spectrum corresponding to α -Ni(OH)₂₋₀, which was attributed to the vibration of the intercalated Cl⁻ (Zhang et al., 2021; Zhang et al., 2020). The decreasing intensity of the Cl⁻ vibration may be related to the decreasing Cl⁻ content in the samples.

3.1.2. Stability of the samples

Fig. 3 displays the comparison of the XRD patterns of the samples from α -Ni(OH)₂₋₀ to α -Ni(OH)₂₋₂₀ before and after being soaked in 6 M KOH solution.

After three days of soaking α -Ni(OH)₂₋₀, the diffraction peaks denoting α -Ni(OH)₂ at about 11°, 22.5°, 33.5°, 39°, and 60° disappeared, and those representing β -Ni(OH)₂ at about 19°, 33°, 38.5°, 52°, 59°, 62.5°, 69.5°, and 72.5° appeared. The conversion of α -Ni(OH)₂₋₀ to β -Ni(OH)₂ was complete.

After three days of soaking Ni-Al LDHs, the XRD pattern of α -Ni(OH)₂₋₅ was such that the diffraction peaks ascribed to α -Ni(OH)₂ at about 11°, 33.5°, 39°, and 60° disappeared and those related to β -Ni(OH)₂ at about 33°, 38.5°, 52°, 59°, 62.5°, 69.5°, and 72.5° appeared. The diffraction peak representing α -Ni(OH)₂ at about 22.5° was retained. For α -Ni(OH)₂₋₁₀ and α -Ni(OH)₂₋₁₅, all the diffraction peaks attributed to α -Ni(OH)₂ were reserved. A diffraction peak of β -Ni(OH)₂ at approximately 52° was observed. A combinative peak of α -Ni(OH)₂ at about 61° and β -Ni(OH)₂ at about 62.5° were exhibited. For α -Ni(OH)₂₋₂₀, the diffraction peaks of α -Ni(OH)₂ at about 11°, 22.5°, and 33.5° were reserved. New peaks

representing α -Ni(OH)₂ at about 39° and 46° were observed. The diffraction peak of α -Ni(OH)₂ at about 60° was split into two peaks located at about 60° and 61°. A combinative peak related to β -Ni(OH)₂ at about 62.5° and 69.5° was observed. It is apparent from the above analysis that the higher the Al content in the fresh sample, the more the α -Ni(OH)₂ content retained after soaking the samples. This was regularly observed among the samples after being soaked for five days, as seen from their XRD patterns in Fig. 3. However, good stability of α -Ni(OH)₂ was only obtained as the Al content in the sample reached to 20%, which was the same as that prepared by chemical precipitation (Jayashree and Kamath, 2011; Liu et al., 1999).

Notably, no recrystallization for the peak representing the (0 0 3) plane (at about 11°) of α -Ni(OH)₂ was detected after its dissolution in pure α -Ni(OH)₂. However, the Ni-Al LDHs exhibited recrystallization by the presence of the (0 0 3) plane. For α -Ni(OH)₂₋₅, the (0 0 3) peak completely disappeared after three days of soaking. However, a faintly visible (0 0 3) peak appeared after being soaked for five days. For α -Ni(OH)₂₋₁₀ to α -Ni(OH)₂₋₂₀, there were already obvious (0 0 3) peaks in their XRD patterns after three days of soaking, which demonstrated the completion of the dissolution process and initiation of the recrystallization process. The intensity of the (0 0 3) peak became stronger from α -Ni(OH)₂₋₅ to α -Ni(OH)₂₋₂₀ after being soaked for the same number of days, implying the ease of dissolution–recrystallization for the (0 0 3) plane with the increasing Al content in the fresh samples.

3.2. Investigation of the electrodeposition process

3.2.1. CV measurement of the electrodeposition systems

Fig. 4 displays the CV curves corresponding to the electrodeposition conducted in the electrolyte with various Al content. An oxidation and reduction reactions occurred during the electrolysis process of the NiCl₂-AlCl₃ solution. The oxidation reaction was related to the anodic reaction of the NiCl₂-AlCl₃ solution. It may include both the formation reaction of chlorine (Eq. (3)) and the decomposition reaction of water (Eq. (4)). According to the anodic reaction of chlor-alkali industry, the formation reaction of chlorine was thought to be the main reaction in the present work. Eq. (3) was, therefore, given in the CV diagram. The reduction reaction was attributed to the evolution of H₂ (Zhang et al., 2020), which was corresponded to the cathodic reaction of the NiCl₂-AlCl₃ solution. Both the anodic and cathodic reactions showed a positive trend with the increasing Al content in the electrolyte. Notably, H⁺ ions were produced from the hydrolysis reactions of Al³⁺ and Ni²⁺, as shown in Eqs. (5) and (6). Thus, Eqs. (7) and (8) were included in the H₂ evolution process. As the cathodic process was dominated by

Table 2 The mass percentage of Cl⁻ in the sample (%).

α -Ni(OH) ₂₋₀	α -Ni(OH) ₂₋₅	α -Ni(OH) ₂₋₁₀	α -Ni(OH) ₂₋₁₅	α -Ni(OH) ₂₋₂₀
3.23	2.44	1.98	1.89	1.92

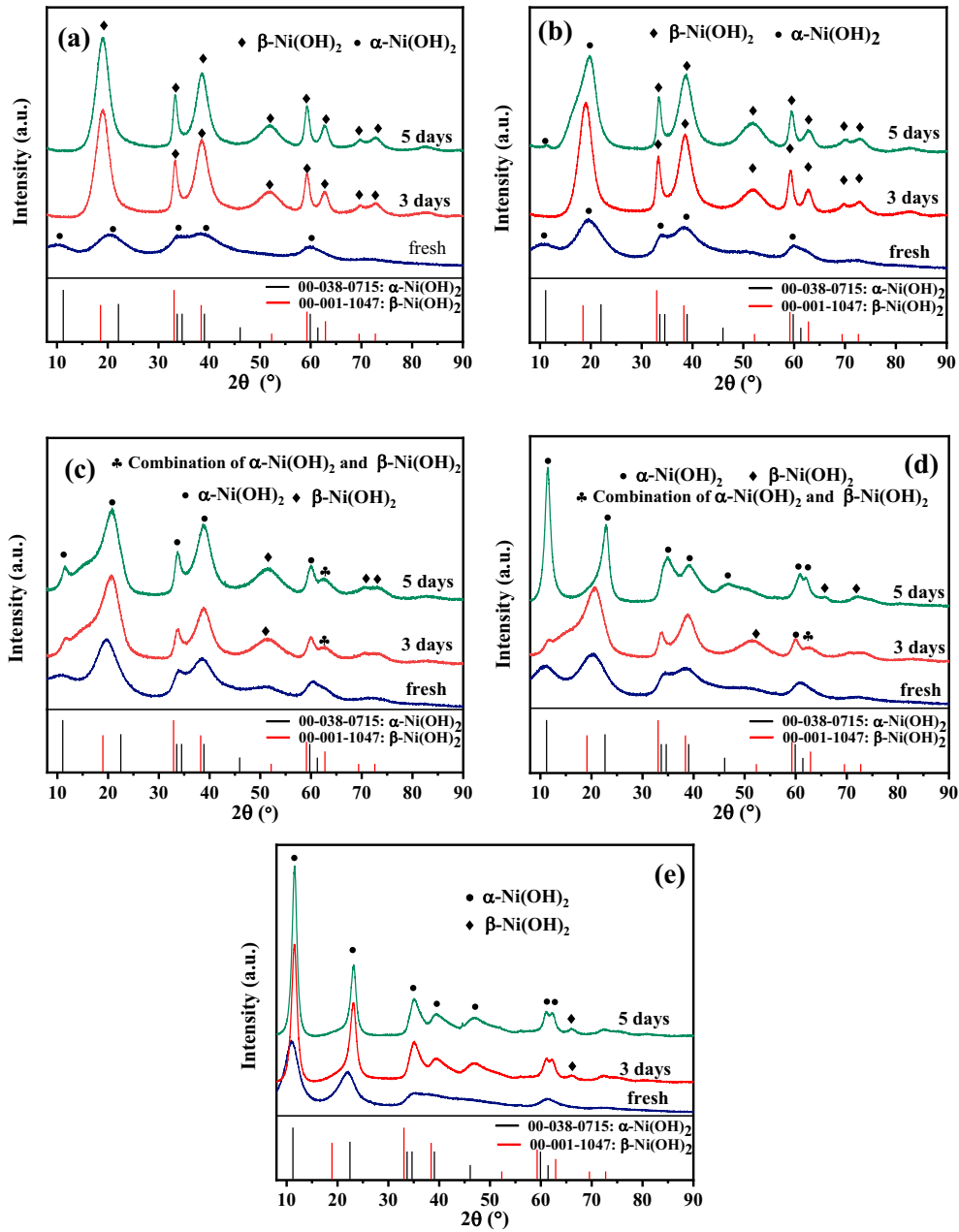
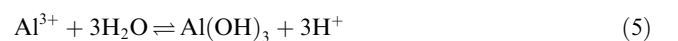


Fig. 3 Comparison of the XRD patterns of the samples before and after being soaked: (a) α -Ni(OH)₂₋₀, (b) α -Ni(OH)₂₋₅, (c) α -Ni(OH)₂₋₁₀, (d) α -Ni(OH)₂₋₁₅ and (e) α -Ni(OH)₂₋₂₀.

Eq. (7), which was also significant to the electrodeposition process, it was represented in the CV diagram.

During the electrodeposition process, the generated OH⁻ ions in Eq. (7) reacted with Al³⁺ and Ni²⁺ in the electrolyte to form precipitates. The precipitation reaction in pure NiCl₂ solution is given by Eq. (9). Based on the pathways for the electrodeposition of Ni-Al LDHs proposed by Gualandi (Gualandi et al., 2015), the precipitation reaction between OH⁻ and Al³⁺-Ni²⁺ in the AlCl₃-NiCl₂ solution may be given by Eqs. (10) and (11). The occurrence of Eq. (10) depends on the formation rate of OH⁻ ions in Eq. (7). Under a fast formation rate, only Eq. (11) takes place. Under a slow rate, Eq. (10) takes place initially followed by Eq. (11) as the solubility product of Al(OH)₃ (1.3×10^{-33}) is lower than that of the LDHs

(between 1.3×10^{-33} for Al(OH)₃ and 5.5×10^{-16} for Ni(OH)₂).



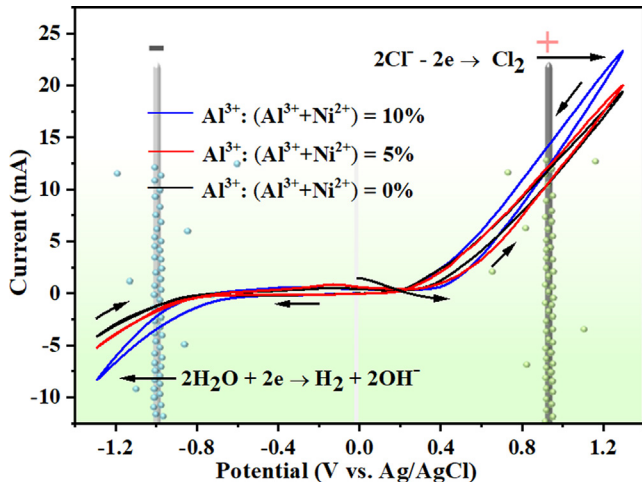
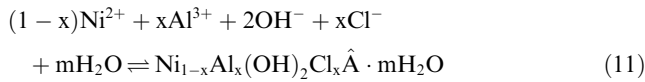
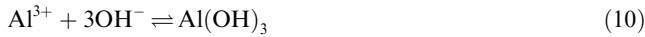
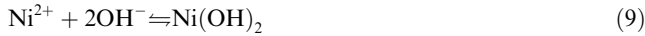


Fig. 4 CV curves for various Al content electrodeposition systems.



3.2.2. Variation of pH in the cathodic chamber

Fig. 5a presents the pH variation curves for the cathodic chamber corresponding to the electrodepositions in electrolytes initially containing 0–20% Al.

Irrespective of the Al content in the initial electrolyte, each pH variation curve was gentle, indicating a slight fluctuation in the property of the electrolyte during electrodeposition. Meanwhile, the pH on each curve increased gradually with the electrodeposition process. It was ascribed to the transportation of OH^- ions from the surface of the cathode.

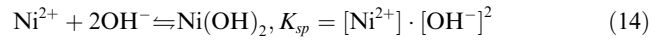
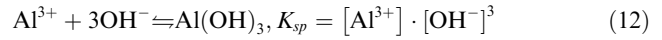
The increasing trend in the catholyte pH of pure NiCl_2 electrolyte (~ 1.0) was more obviously than that of $\text{AlCl}_3\text{-NiCl}_2$ electrolyte (~ 0.5), as shown in Fig. 5a. In addition, the pH value of the Al-containing electrolyte was much lower than that of the pure NiCl_2 solution. The lower pH of the initial Al-containing electrolytes can be attributed to the reaction given by Eq. (4). However, low levels of catholyte pH in Al-containing electrolytes during electrodeposition are contrary to our previous observations (Zhang et al., 2020).

In our previous work, hydrochloric acid was used to acidify the catholyte (pure NiCl_2 solution) to different pH values. The results demonstrated that the pH of acidified catholyte reached a value almost equal to that of the unacidified electrolyte after electrodeposition for five minutes. Later, there was no visible difference in the catholyte pH of acidified and unacidified electrolytes.

The above comparisons led to the investigation of the nature of the catholyte pH variation during electrodeposition in both NiCl_2 and $\text{AlCl}_3\text{-NiCl}_2$ solutions.

During the electrodeposition process, the OH^- concentration ($[\text{OH}^-]$) required to precipitate $\text{Al}(\text{OH})_3$ (Eq. (13)) was calculated from its solubility product (K_{sp} , Eq. (12)), and that

needed to precipitate $\text{Ni}(\text{OH})_2$ (Eq. (15)) was obtained from Eq. (14).



Hereafter, the relationship between the pH of the solution and $[\text{OH}^-]$ (Eq. (17)) was obtained by considering the ionic product of water (K_w , Eq. (16)) into the pH calculation formula (Eq. (17)).



$$\text{pH} = -\lg[\text{H}^+] = 14 + \lg[\text{OH}^-] \quad (17)$$

Incorporating Eqs. (13) and (15), K_{sp} values of 1.3×10^{-33} for $\text{Al}(\text{OH})_3$ and 5.5×10^{-16} for $\text{Ni}(\text{OH})_2$ into Eq. (17), the correlations of pH with Al^{3+} ($\text{pH} - [\text{Al}^{3+}]$) and Ni^{2+} ($\text{pH} - [\text{Ni}^{2+}]$) concentrations for precipitating $\text{Al}(\text{OH})_3$ and $\text{Ni}(\text{OH})_2$ (Eqs. (18) and (19)) were obtained. Fig. 5b and c are curves for these correlations.

$$\text{pH} = 3.038 - \frac{1}{3} \lg[\text{Al}^{3+}] \quad (18)$$

$$\text{pH} = 6.37 - \frac{1}{2} \lg[\text{Ni}^{2+}] \quad (19)$$

Notably, there was a separation of 2.5 cm between the pH metric point and cathode sheet. The pH values in Fig. 5a were thus considered to belong to the bulk solution. The OH^- ions were mainly originated by the transportation of OH^- from the cathodic surface. Thus, its formation rate was considered to be slow. Based on the electrodeposition pathway given by Gualandi (Gualandi et al., 2015), the initial precipitate reaction in the $\text{AlCl}_3\text{-NiCl}_2$ electrolyte was given by Eq. (10).

On turning the power on, the H^+ ions initially generated by Eqs. (5) and (6) in both the $\text{AlCl}_3\text{-NiCl}_2$ and pure NiCl_2 solutions were immediately consumed either by Eq. (8) or (20). The hydrolysis reactions (Eqs. (5) and (6)) in the bulk solution moved toward the right. Meanwhile, the concentrations of Al^{3+} and Ni^{2+} decreased as the precipitation proceeded forward, which caused the hydrolysis reactions to move toward the left direction. The tendency of the hydrolysis reaction to move to the left was greater than that to the right due to the lower concentrations of Al^{3+} and Ni^{2+} ions compared to that in the initial electrolyte. The synergistic effect of these two factors on the hydrolysis reaction slightly increased the catholyte pH in the bulk solution during the electrodeposition process. When the OH^- ions were transported from the cathodic surface to the bulk solution, the local pH further increased.



In the $\text{AlCl}_3\text{-NiCl}_2$ electrolyte, Al^{3+} was precipitated initially with the increasing pH value. Once the catholyte pH was raised to the level required to form the $\text{Al}(\text{OH})_3$ precipitate, Al^{3+} began to react with OH^- , preventing the local pH from increasing further. Regardless of acidification, as the free H^+ was consumed and OH^- concentration was increased in

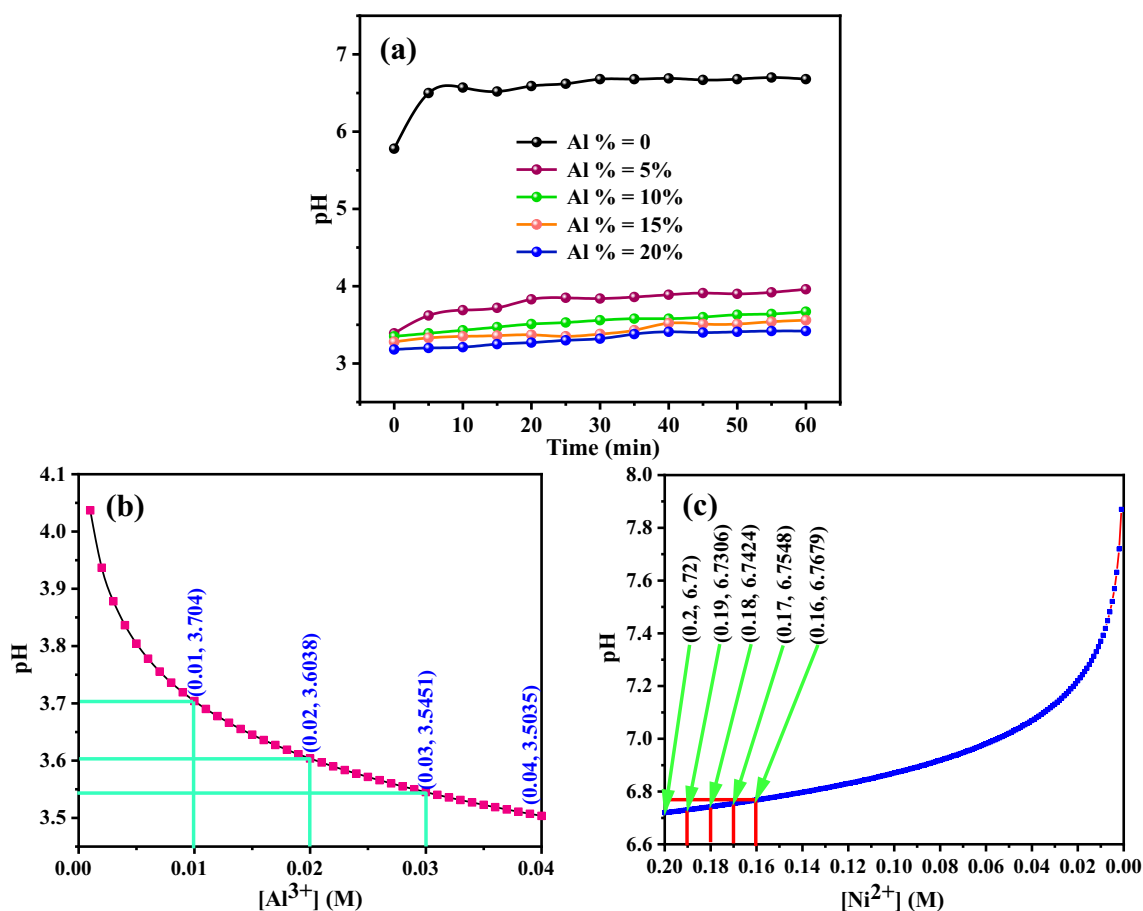


Fig. 5 (a) pH variation during the electrodepositions in electrolytes initially containing different Al concentrations, (b) and (c) the relationships of pH-[Al³⁺] and pH-[Ni²⁺].

pure NiCl₂ electrolyte, Ni²⁺ was precipitated with OH⁻ to prevent the increase in the pH of the electrolyte. The pH level required to form the precipitate were at least 6.72, 3.704, 3.60, 3.704, 3.6038, 3.5451, and 3.5035 for pure NiCl₂ solution (0.2 M), and electrolytes with the initial Al contents of 5% (0.19 M NiCl₂ + 0.01 M AlCl₃), 10% (0.18 M NiCl₂ + AlCl₃), 15% (0.17 M NiCl₂ + 0.03 M AlCl₃) and 20% (0.16 M NiCl₂ + 0.04 M AlCl₃), as shown in Fig. 5b and c. The pH required to precipitate for Al-containing electrolytes was obviously much lower than that for pure NiCl₂ solution. Thus, the pH level of the Al-containing electrolytes was much lower than that of the pure NiCl₂ solution during electrodeposition, as seen from Fig. 5a.

3.2.3. Electrodeposition yield and current efficiency

Fig. 6 shows the electrodeposition yield and current efficiency for the electrodepositions conducted in electrolytes initially containing 0–20% Al. In addition to the reactions mentioned in CV part, complex dissolution reactions of the precipitate in the chloride solution may be also involved. Thus, the electrodeposition yield was a result of the synergistic effect of various precipitation reactions and the dissolution reactions of the precipitate. The observation was recorded thrice, and the ending result was taken as the average of the three readings.

From the XRD patterns in Fig. 2b, no obvious diffraction peak corresponding to Al(OH)₃ was detected, demonstrating

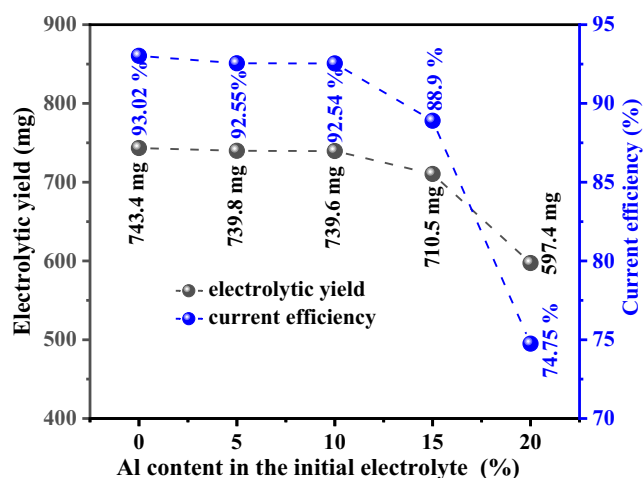


Fig. 6 Electrolytic yield and current efficiency of various electrodeposition systems.

there was no Al(OH)₃ in the sample. Thus, the current efficiency was calculated based on the precipitate reaction of Eq. (11). The calculating formula used was given below (Shi et al., 2020).

$$\eta = \frac{NF \cdot n_{Ni-AILDHs}}{It} \times 100\% = \frac{NF \cdot m_{Ni-AILDHs}/M_{Ni-AILDHs}}{It} \times 100\% \quad (21)$$

where, N denotes the number of electrons transferred per mole precipitate. According to Eq. (11), N equals to 2. $n_{Ni-AILDHs}$ denotes the amount of substance for the Ni-Al LDHs (mol). F represents the Faraday's constant (96500C/mol). I is the current intensity applied (0.42 A). t denotes the electrodeposition time (3600 s). $m_{Ni-AILDHs}$ denotes the total mass of the precipitate (g). $M_{Ni-AILDHs}$ denotes the molar mass of the Ni-Al LDHs. Because α -Ni(OH)₂ is non-stoichiometric (Huang et al., 2018), the molar mass of the Ni-Al LDHs cannot correspond to an exact value. Based on the XRD results, the molar mass of the sample was set as 106.2 g/mol for α -Ni(OH)₂·0.75H₂O for calculation.

The Al content in the initial electrolyte showed no obvious influence on the electrodeposition yield and current efficiency when it ranged of 0–10% (Fig. 6). However, the electrodeposition yield and current efficiency decreased from (739.6 mg, 92.54%) to (710.5 mg, 88.9%) as the initial Al content increased from 10% to 15%. In particular, there was a dramatic decrease from (710.5 mg, 88.9%) to (597.4 mg, 74.75%) as the initial Al content increased from 15% to 20%. The increasing Al content and decreasing Ni content in the precipitate (as seen from Fig. 2a) were apparently responsible for the decline as the former was lighter than the latter. In addition, the diffusion of complex ions into the bulk solution prior to precipitation could be another reason for the decline.

Streinz reported a possibility for the preferential formation of some Ni complex ions, such as Ni₄(OH)₄⁴⁺, during the electrodeposition of Ni(OH)₂ from Ni(NO₃)₂ solution and proposed a two-step precipitation reaction for the process (Eqs. (22) and (23)) (Streinz et al., 1995). The current inefficiency in the condensed Ni(NO₃)₂ solution was attributed to the diffusion of Ni₄(OH)₄⁴⁺ toward the bulk solution which weakened the occurrence of Eq. (23). This explanation for current

inefficiency in concentrated solution was found to be suitable for the present case. With the increasing Al content in the electrolyte, the solubility product constant for the Ni-Al LDHs was closer to that of Al(OH)₃. Thus, the precipitation reaction of Ni-Al LDHs was easier. When the formation rate of OH⁻ was identical, more complex ions similar to Ni₄(OH)₄⁴⁺ were formed at the same time in high Al-containing electrolytes. Thus, a high concentration difference in the complex ions was observed between the cathodic surface and bulk solution, which was beneficial for the transportation of complex ions toward the bulk solution and detrimental to the efficient utilization of OH⁻ ions. Thus, a current inefficiency was found to occur in high Al-containing electrolytes.



3.2.4. Separations in the electrodeposition patterns caused by the Al content

Fig. 7 shows the images of the cathodic chamber for various initial Al content electrodeposition systems.

When the initial Al content in the electrolyte was 0%, the synthesized precipitate was partially attached to the cathode sheet and partially scraped down to the bottom of the cathodic chamber as seen from Fig. 7a. When the initial Al content in the electrolyte increased to 5%, there was obviously less precipitate scraped down to the cathodic chamber as shown in Fig. 7b, indicating more precipitate was attached to the cathode sheet. While, the precipitate on the cathode surface was not tightly attached. When the cathode sheet was removed from the electrolyte, part of the attached precipitate fell off, leaving a thin layer of precipitate attached on the most areas of the cathode sheet as seen from Fig. 7b. When the initial Al content in the electrolyte increased to 10%, the amount of precipitate falling to the bottom of the cathodic chamber was further reduced. As seen from Fig. 7c, there was virtually

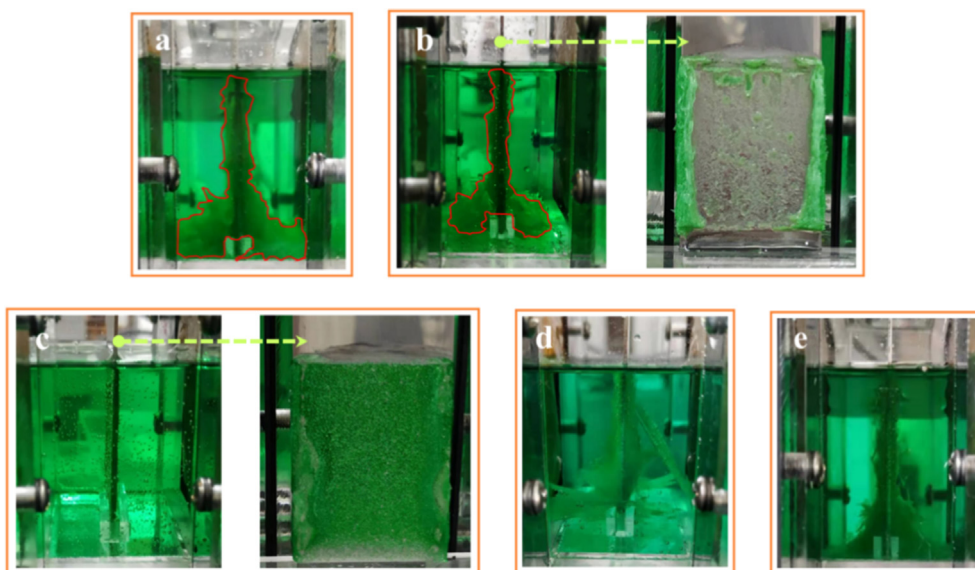


Fig. 7 Images of the cathodic chamber for various initial Al content electrodeposition systems: (a) 0%, (b) 5%, (c) 10%, (d) 15% and (e) 20%.

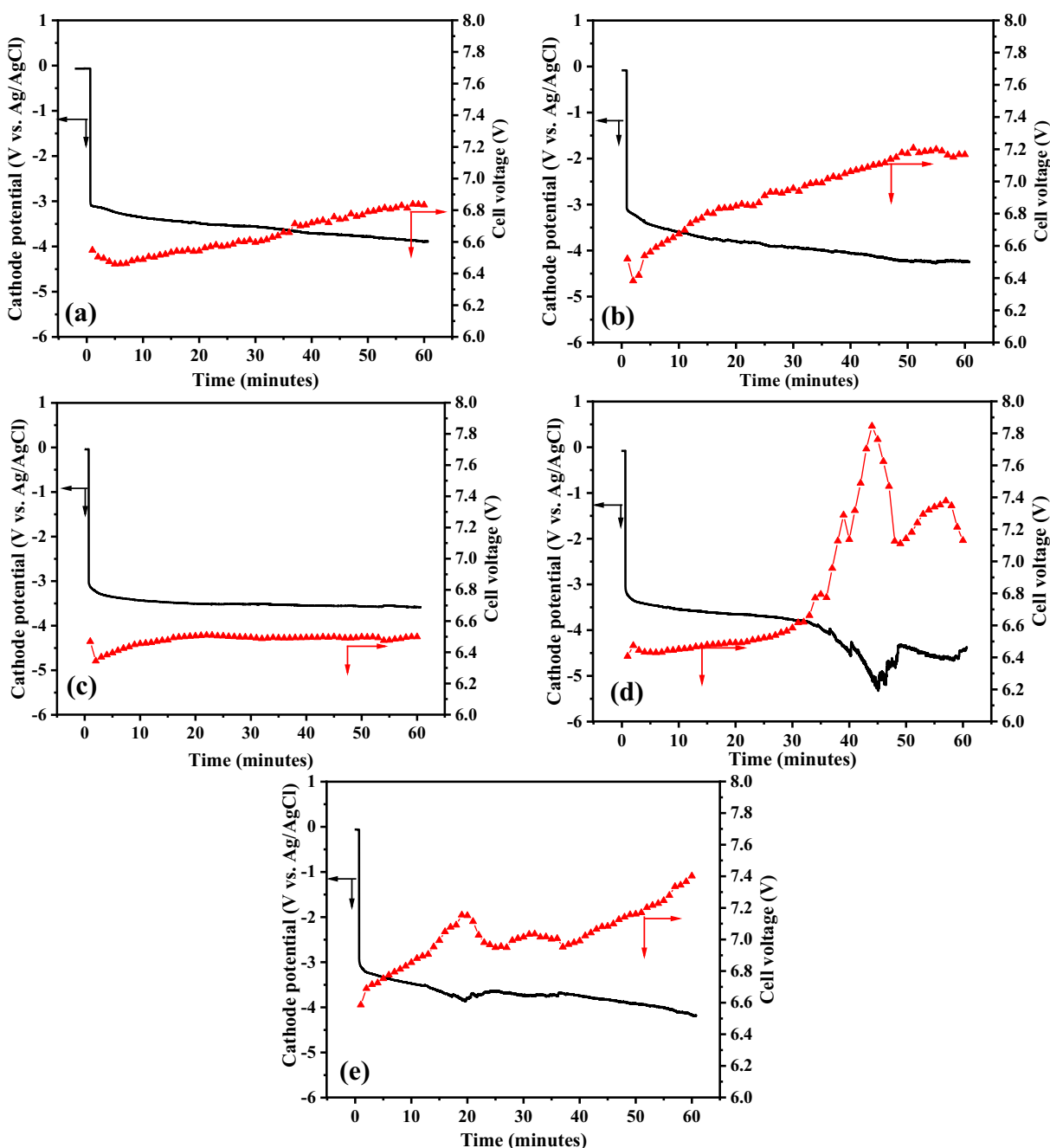


Fig. 8 Cell voltage and cathode potential vs. Ag/AgCl for electrodepositions in various Al content electrolytes: (a) 0%, (b) 5%, (c) 10%, (d) 15% and (d) 20%.

no precipitate at the bottom of the cathodic chamber, and the precipitate was densely attached to the cathode sheet in a spongy-like shape, leaving many bare and minute areas on the cathode surface.

The observations above demonstrate that the electrodeposition pattern gradually developed to the in-situ mode when the initial Al content in the electrolyte increased from 0 to 10%. When the initial Al content in the electrolyte was 10%, the electrodeposition became an in-situ process.

When the initial Al content in the electrolyte was increased to 15%, precipitate can be seen both on cathode surface and the bottom of the cathodic chamber as seen from Fig. 7d.

However, because the connections between the precipitates and the cathode and between the precipitates were relatively tight, the precipitate fell off from the cathode in large pieces. When the initial Al content in the electrolyte increased to 20%, the connections between the precipitates and the cathode and between the precipitates became loose, the precipitate fell off from the cathode sheet in clastic pieces as shown in Fig. 7e.

The observations above indicate that the electrodeposition pattern deviated from in-situ process when the initial Al content in the electrolyte increased from 10% to 20%.

The electrodeposition pattern not only affects the cell voltage but also affects the potential of the cathode sheet itself.

Fig. 8 shows the cell voltage and cathode potential vs. Ag/AgCl for the electrodeposition in electrolytes with Al content in the range of 0–20%.

For each electrodeposition system, the shapes of the two curves are almost symmetrical, indicating that the fluctuation of the cell voltage is mainly caused by the reactions taking place in the cathodic chamber. Both the curves are relatively gentle for electrodeposition in electrolytes with initial Al content lower than 10% and fluctuate a lot in electrolytes with initial Al content in the range of 15–20%. The cell voltage became higher and the cathode potential became more negative with the electrodeposition progress. It can be ascribed to the decreasing electrolyte concentration and increasing amount of precipitate attached to the cathode. The attached precipitate was unfavorable to the conductivity of the cathode sheet and ion transfer from the nearby cathode to its surface. When the electrodeposition was conducted in electrolyte with initial Al content of 10%, the bare minute-areas formed by the tightly attached precipitate not only ensured the conductivity of the cathode but also provided channels for ion transport from the nearby cathode to its surface. Thus, the cell voltage was increased slightly and the cathode potential slightly changed to be more negative as seen from Fig. 8c. When the electrodeposition was conducted in electrolyte with initial Al content of 15%, the falling of the large-piece-like precipitate led to dramatic fluctuations in the cathodic potential and cell voltage as seen from Fig. 8d. When the initial Al content in the electrolyte increased to 20%, the precipitate was scraped off the cathode surface in clastic-like shape (Fig. 7e). That is, the scraping-off process of the precipitate became easier than that in electrolyte initially containing 15% Al. Therefore, there were less fluctuations observed in both curves (Fig. 8e).

4. Conclusions

Ni-Al LDHs was synthesized from NiCl₂-AlCl₃ solution by electrodeposition. The Al contents in the samples were slightly higher than that in the raw materials. With the increasing Al content in the sample, the crystallinity and interlayer spacing increased and decreased, respectively. Also, the preferred orientations of (0 0 3) and (0 0 6) were observed. The dissolution–recrystallization of the (0 0 3) plane was observed on soaking the Ni-Al LDHs in an alkali solution. The dissolution–recrystallization process was easier as the Al content in the initial Ni-Al LDHs increased. During electrodeposition, there was a slight fluctuation in the catholyte pH. The pH value decreased with the increasing Al content in the initial electrolyte. When the Al content in the initial electrolyte was higher than 10%, the electrodeposition yield and current efficiency decreased obviously with the increasing initial Al content in the electrolyte. When the initial Al content in the electrolyte was 10%, the electrodeposition was an in-situ process. For electrolytes with initial Al content in the range of 0–10% and 10–20%, the electrodeposition separately developed toward and off the in-situ process.

5. Authors' contributions*a

Ting-an Zhang and Junjie Zhang discussed the experimental design and analyzed the feasibility. Junjie Zhang did the exper-

iments. Junjie Zhang and Sen feng analyzed the data collected and wrote this manuscript.

Declaration of Interest Statement

No conflict of interest exists in the submission of this manuscript, which is approved by all authors for publication. We would like to declare that the work described was original research, which has not been published previously, and not under consideration for publication elsewhere, in whole or in part.

Acknowledgement

This study was financially supported by the National Natural Science Foundation of China (No. U1710257).

References

- Ash, B., Mishra, K.G., Subbaiah, T., Paramguru, R.K., Mishra, B.K., 2015. Electrochemical studies on electrolytic preparation of battery grade nickel hydroxide-Effect of (OH⁻) to Ni²⁺ ratio. *J. Power Sources* 275, 55–63.
- Chen, H., Wang, J.M., Pan, T., Xiao, H.M., Zhang, J.Q., Cao, C.N., 2002. Effects of coprecipitated zinc on the structure and electrochemical performance of Ni/Al-layered double hydroxide. *Int. J. Hydrogen Energy* 27, 489–496.
- Cheng, F.Y., Chen, J., Shen, P.W., 2005. Y(OH)₃-coated Ni(OH)₂ tube as the positive-electrode materials of alkaline rechargeable batteries. *J. Power Sources* 150, 255–260.
- Demourgues Guerlou, L., Delmas, C., 1993. Structure and properties of precipitated nickel-iron hydroxides. *J. Power Sources* 45, 281–289.
- Demourgues Guerlou, L., Delmas, C., 1996. Electrochemical behavior of the manganese-substituted nickel hydroxide. *J. Electrochem. Soc.* 143, 561–567.
- Fang, K.L., Chen, M.F., Chen, J.Z., Tian, Q.H., Wong, C.P., 2019. Cotton stalk-derived carbon fiber@Ni-Al layered double hydroxide nanosheets with improved performances for supercapacitors. *J. Appl. Surf. Sci* 475, 372–379.
- Gualandi, I., Monti, M., Scavetta, E., Tonelli, D., Prevot, V., Mousty, C., 2015. Electrodeposition of layered double hydroxides on platinum: Insights into the reactions sequence. *Electrochim. Acta* 152, 75–83.
- Hou, Z.Q., Tian, F.S., Gao, Y.P., Wu, W., Yang, L.X., Jia, X.L., Huang, K.J., 2018. Nickel cobalt hydroxide/reduced graphene oxide/carbon nanotubes for high performance aqueous asymmetric supercapacitors. *J. Alloy. Compd.* 753, 525–531.
- Hu, M., Yang, Z.Y., Lei, L.X., Sun, Y.M., 2011. Structural transformation and its effects on the electrochemical performances of a layered double hydroxide. *J. Power Sources* 196, 1569–1577.
- Huang, H.L., Guo, Y.J., Cheng, Y.H., 2018. Ultrastable α phase nickel hydroxide as energy storage materials for alkaline secondary batteries. *Appl. Surf. Sci.* 435, 635–640.
- Jayashree, R.S., Kamath, P.V., 2011. Suppression of the α - β -nickel hydroxide transformation in concentrated alkali: Role of dissolved cations. *J. Appl. Electrochem.* 31, 1315–1320.
- Jayashree, R.S., Vishnu, K.P., 1999. Factors governing the electrochemical synthesis of α -nickel (II) hydroxide. *J. Appl. Electrochem.* 29, 449–454.
- Jayashree, R.S., Vishnu, K.P., 2001. Nickel hydroxide electrodeposition from nickel nitrate solutions: mechanistic studies. *J. Power Sources* 93, 273–278.
- Li, J.L., Aslam, M.K., Chen, C.G., 2018. One-pot hydrothermal synthesis of porous α -Ni(OH)₂/C composites and its application in

- Ni/Zn alkaline rechargeable battery. *J. Electrochem. Soc.* 165, A910–A917.
- Li, H., Ma, J., Evans, D.G., Zhou, T., Li, F., Duan, X., 2016. Molecular dynamics modeling of the structures and binding energies of α -nickel hydroxides and nickel-aluminum layered double hydroxides containing various interlayer guest anions. *Chem. Mater.* 18, 4405–4414.
- Li, Y.W., Yao, J.H., Liu, C.J., Zhao, W.M., Deng, W.X., Zhong, S.K., 2010. Effect of interlayer anions on the electrochemical performance of Al-substituted α -type nickel hydroxide electrodes. *Int. J. Hydrogen Energy* 35, 2539–2545.
- Li, Y.W., Yao, J.H., Zhu, Y.X., Zou, Z.G., Wang, H.B., 2012. Synthesis and electrochemical performance of mixed phase α/β nickel hydroxide. *J. Power Sources* 203, 177–183.
- Liu, C.C., Chen, Q.Y., Hao, Q.Y., Zheng, X.R., Li, S.Y., Jia, D.B., Gong, T., Liu, H., Zhang, J., 2019. Ni(OH)₂/NiSe₂ hybrid nanosheet arrays for enhanced alkaline hydrogen evolution reaction. *Int. J. Hydrogen Energy* 44, 4832–4838.
- Liu, B., Wang, X.Y., Yuan, H.T., Zhang, Y.S., Song, D.Y., Zhou, Z. X., 1999. Physical and electrochemical characteristics of aluminum-substituted nickel hydroxide. *J. Appl. Electrochem.* 29, 855–860.
- Liu, B., Yuan, H.T., Zhang, Y.S., Zhou, Z.X., Song, D.Y., 1999. Cyclic voltametric studies of stabilized α -nickel hydroxide. *J. Power Sources* 79, 277–280.
- Miao, C.C., Zhu, Y.J., Huang, L.G., Zhao, T.Q., 2015. The relationship between structural stability and electrochemical performance of multi-element doped alpha nickel hydroxide. *J. Power Sources* 274, 186–193.
- Murthy, M., Nagarajan, G.S., Weidner, J.W., Van Zee, J.W., 1996. A model for galvanostatic deposition of nickel hydroxide. *J. Electrochem. Soc.* 143, 2319–2327.
- Nethravathi, C., Ravishankar, N., Shivakumara, C., Rajamathi, M., 2007. Nanocomposites of α -hydroxides of nickel cobalt by delamination and co-stacking: enhanced stability of α -motifs in alkaline medium and electrochemical behavior. *J. Power Sources* 172, 970–974.
- Pan, T., Wang, J.M., Zhao, Y.L., Chen, H., Xiao, H.M., Zhang, J.Q., 2003. Al-stabilized α -nickel hydroxide prepared by electrochemical impregnation. *Mater. Chem. Phys.* 78, 711–718.
- Peng, Y., Chen, J., Jiang, L.X., Wang, T.Y., Yang, H.C., Liu, F.Y., Jia, M., 2020. Preparation of Sb₂O₃/Sb₂S₃/FeOOH composite photoanodes for enhanced photoelectrochemical water oxidation. *Trans. Nonferrous Met. Soc. China* 30, 1625–1634.
- Sasaki, Y., Yamashita, T., 1998. Effect of electrolytic conditions on the deposition of nickel hydroxide. *Thin Solid Films* 334, 117–119.
- Shangguan, E.B., Li, J., Guo, D., Guo, L.T., Nie, M.Z., Chang, Z.R., Yuan, X.Z., Wang, J.A., 2015. A comparative study of structural and electrochemical properties of high-density aluminum substituted α -nickel hydroxide containing different interlayer anions. *J. Power Sources* 282, 158–168.
- Shi, Y., Jiang, K.X., Zhang, T.A., 2020. A Cleaner electrolysis process to recover alumina from synthetic sulfuric acid leachate of coal fly ash. *Hydrometallurgy* 191, 105196.
- Streinz, C.C., Motupally, S., Weidner, J.W., 1995. The effect of temperature and ethanol on the deposition of nickel hydroxide films. *J. Electrochem. Soc.* 142, 4051–4056.
- Subbaiah, T., Mallic, S.C., Mishra, K.G., Sanjay, K., Das, R.P., 2002. Electrochemical precipitation of nickel hydroxide. *J. Power Sources* 112, 562–569.
- Vishnu Kamath, P., Kumar, G., Munichandraiah, N., Shukla, A.K., Ganesh Kumar, V., Munichandraiah, N., 1994. Stabilized α -Ni(OH)₂ as electrode material for alkaline secondary cells. *J. Electrochem. Soc.* 141, 2956–2959.
- Wang, L.Q., Li, X.C., Guo, T.M., Yan, X.B., Tay, B.K., 2014. Three-dimensional Ni(OH)₂ nanoflakes/graphene/nickel foam electrode with high rate capability for supercapacitor applications. *Int. J. Hydrogen Energy* 39, 7876–7884.
- Xia, Y., Zhong, H.Y., Fang, R.Y., Liang, C., Xiao, Z., Huang, H., Gan, Y.P., Zhang, J., Tao, X.Y., Zhang, W.K., 2018. Biomass derived Ni(OH)₂@porous carbon/sulfur composites synthesized by a novel sulfur impregnation strategy based on supercritical CO₂ technology for advanced Li-S batteries. *J. Power Sources* 378, 73–80.
- Yao, J.H., Li, Y.W., Li, Y.X., Zhu, Y.X., Wang, H.B., 2013. Enhanced cycling performance of Al-substituted α -nickel hydroxide by coating with β -nickel hydroxide. *J. Power Sources* 224, 236–240.
- Yao, K.L., Zhai, M.H., Ni, Y.H., 2019. α -Ni(OH)₂·0.75H₂O nanofilms on Ni foam from simple NiCl₂ solution: fast electrodeposition, formation mechanism and application as an efficient bifunctional electrocatalyst for overall water splitting in alkaline solution. *Electrochim. Acta* 301, 87–96.
- Yuan, P.W., Guo, S.H., Gao, S.Q., Wang, J., Chen, W.Q., Li, M., Ma, K.Y., Wang, N., Liu, F., Cheng, J.P., 2019. Influence of Ni/Cu ratio in nickel copper carbonate hydroxide on the phase and electrochemical properties. *J. Alloy. Compd.* 780, 147–155.
- Zhang, J.J., Zhang, T.A., Feng, S., 2020. α -Ni(OH)₂ electrodeposition from NiCl₂ solution. *Trans. Nonferrous Met. Soc. China* 30, 2802–2811.
- Zhang, J.J., Zhang, T.A., Feng, S., 2021. Mechanism Investigation of α -Ni(OH)₂ Electrodeposition from a NiCl₂ Solution. *Int. J. Hydrogen Energy* 46, 41–49.